ACS OMEGA

http://pubs.acs.org/journal/acsodf

Article

Scalable Synthesis of a Sub-10 nm Chalcopyrite ($CuFeS_2$) Nanocrystal by the Microwave-Assisted Synthesis Technique and Its Application in a Heavy-Metal-Free Broad-Band Photodetector

Brajesh Kumar,[§] Satya Veer Singh,[§] Abhimanyu Chattopadhyay, Sajal Biring,* and Bhola N. Pal*

Cite This: *ACS Omega* 2020, 5, 25947−25953

Read Online

ACCESS | Metrics & More | Article Recommendations

ABSTRACT: A heavy-metal-free chalcopyrite ($CuFeS_2$) nanocrystal has been synthesized via microwave-assisted growth. Large-scale nanocrystals with an average particle size of 5 nm are fabricated by this technique within a very short period of time without any need for organic ligands. Scanning electron microscopy study (SEM) of individual synthesis steps indicates that aggregates of nanocrystals are formed as flakes during microwave-assisted synthesis. The colloidal solution of the $CuFeS_2$ nanocrystal was prepared by sonicating these flakes. Transmission electron microscopy (TEM) study reveals the growth of sub-10 nm $CuFeS_2$ nanocrystals that are further characterized by X-ray diffraction. UV−visible absorption spectroscopic study shows that the band gap of this nanocrystal is ∼1.3 eV. To investigate the photosensitive nature of this nanocrystal, a bilayer p−n heterojunction photodetector has been fabricated using this nontoxic $CuFeS_2$ nanocrystal as a photoactive material and n-type ZnO as a charge-transport layer. The detectivity of this photodetector reaches above 10^{12} Jones in visible and near-infrared (NIR) regions under 10 V external bias, which is significantly high for a nontoxic nanocrystal-based photodetector.

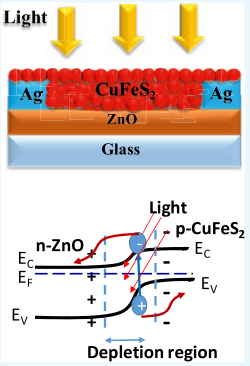

1. INTRODUCTION

In the last two decades, a variety of colloidal nanocrystals have been developed, which have been used in different areas of electronics and optoelectronics including light-emitting diodes, photodetectors, solar cells, etc.[1−4] However, most of these high-performing colloidal nanocrystals are heavy-metal based, which poses a big concern for the environment and health.[5,6] Besides these electronic applications, different biomedical applications require nontoxic nanocrystals.[7−10] Therefore, development of earth-abundant, nontoxic, and eco-friendly nanocrystal materials is of utmost importance.[11−13] Accordingly, a large variety of different heavy-metal-free nanocrystals have been developed including Cu_2ZnSnS_4 (CZTS),[14] $CuInS_2$ (CIS),[9,14] CuInZnS (CIZS),[15] Cu_2SnS_3,[16] and $CuFeS_2$.[17] Among them, chalcopyrite ($CuFeS_2$) is one of the important materials for both optoelectronic and biomedical applications. This $CuFeS_2$ is one of the most earth-abundant ores showing semiconducting behavior. The optical band gap of this semiconductor is ∼0.55 eV, which can be increased above 1.0 eV by reducing the particle size of the nanostructured $CuFeS_2$.[17,18] Therefore, there is a good opportunity to use $CuFeS_2$ nanoparticles for photovoltaic and broad-band photodetector applications.[19]

Among the different optoelectronic devices, photodetectors have generated a great deal of interest due to their various applications in the fields of optical readers, photomultiplier tubes, remote sensing, photonic circuits, robotics, thermography, spectrometers, astronomy, cameras, optical communication, cell phones, etc.[20,21] Currently, most of the nanocrystal-based photodetectors are fabricated either from toxic elements like lead (Pb),[22,23] cadmium (Cd),[24,25] and mercury (Hg)[26] or from elements that are not earth-abundant.[27,28] Chalcopyrite ($CuFeS_2$) is an ore of copper and has elements in Cu^{1+}/Cu^{2+}, Fe^{3+}/Fe^{2+}, and S^{2-} oxidation states that can overcome both these problems.[29] $CuFeS_2$ has a tetragonal crystal structure that is closely related to zinc blend (Figure 1a). Moreover, $CuFeS_2$ is a direct band gap compound semiconductor with elements belonging to I−III−VI groups.[30] These unique combinations of electrical and optical properties of $CuFeS_2$ make it a versatile material for applications in different fields including batteries, solar cells, LEDs, and thermoelectric, spintronic, and photoelectrochemical cells.[31−33] Nevertheless, there are very few reports on $CuFeS_2$ as an active material in the fabrication of a solar cell or photodetector.[34,35] This is due to the presence of the 3d orbitals of Fe that create an interband [IB] between the valence band [VB] and the conduction band [CB] of $CuFeS_2$.[33] The energy gap between VB and IB is 0.53 eV and indirect in nature, which is not efficient for light absorption.[33]

Received: July 12, 2020
Accepted: September 17, 2020
Published: September 30, 2020

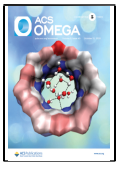

https://dx.doi.org/10.1021/acsomega.0c03336
ACS Omega 2020, 5, 25947−25953

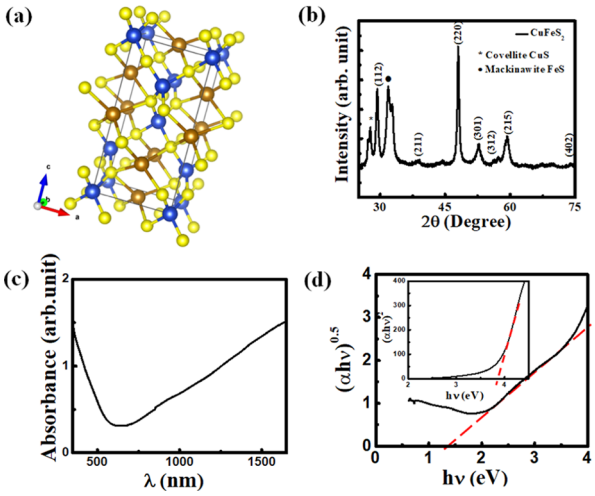

Figure 1. (a) Crystal structure of $CuFeS_2$. Blue, brown, and yellow colors represent Cu, Fe, and S atoms, respectively. (b) X-ray diffraction (XRD) pattern of a $CuFeS_2$ nanocrystal, (c) solution-phase absorption spectrum of a $CuFeS_2$ nanocrystal, and (d) Tauc's plot that has been used to determine the indirect band gap. Inset: Tauc's plot that has been used to determine the direct band gap.

In this work, we present a scalable microwave-assisted synthesis technique that is capable of synthesizing a sub-10 nm $CuFeS_2$ nanocrystal within a few minutes. This synthesized $CuFeS_2$ nanocrystal does not contain any organic ligand and exhibits a strong quantum confinement effect with an enhanced optical band gap of 1.3 eV. A bilayer heterojunction photodetector fabricated using this $CuFeS_2$ nanocrystal as an active material shows good photosensitivity in the visible region of light. In this device structure, a zinc oxide (ZnO) layer has been used as an electron-transport layer, whereas $CuFeS_2$ works as a photoactive material.

2. RESULTS AND DISCUSSION

2.1. X-ray Diffraction (XRD). The crystal phase of a $CuFeS_2$ nanocrystal has been identified by X-ray diffraction (XRD) study. For this study, an XRD sample has been prepared by drop-casting method on a Si substrate. Figure 1b shows the XRD pattern of the $CuFeS_2$ nanocrystal, which indicates intense peaks at $2\theta \sim 29.32$, 48.01, and 57.18 corresponding to the diffraction planes of (112), (220), and (312), respectively. These diffraction peaks confirm the formation of a tetragonal lattice structure of the $CuFeS_2$ nanocrystal (JCPDS file no. 83-0983). Besides, impurity phases of FeS and CuS are observed in XRD data.

2.2. Ultraviolet−Visible (UV−vis) Absorption. The UV−vis absorption study of a $CuFeS_2$ nanocrystal has been performed in a colloidal solution phase by dispersing in a dimethylformamide (DMF) solution. The absorption spectrum shown in Figure 1c indicates that $CuFeS_2$ nanocrystals have strong absorption in the visible to the near-infrared (NIR) region. Considering the $CuFeS_2$ nanocrystal as an indirect band gap semiconductor, the optical band gap of the synthesized nanocrystal has been calculated from Tauc's plot (Figure 1d), which is ~1.3 eV.[18,34] The widening of the band gap of $CuFeS_2$ nanocrystals with respect to its bulk structure is due to the strong quantum confinement effect. A Tauc's plot is also shown in the inset of Figure 1d by considering the $CuFeS_2$ nanocrystal as a direct band gap material that shows a band gap of 3.8 eV, can be responsible for the absorption of high energy photons only. Since the XRD data shows the existence of the CuS impurity phase, plasmonic absorption of the CuS impurity that normally exists within the range of 900−1500 nm can overlap with $CuFeS_2$ absorption.[36−38]

2.3. Scanning Electron Microscopy (SEM) and Transmission Electron Microscopy (TEM). A scanning electron microscopy (SEM) study has been performed in an as-grown $CuFeS_2$ nanocrystal, which is shown in Figure 2a. A thin-film

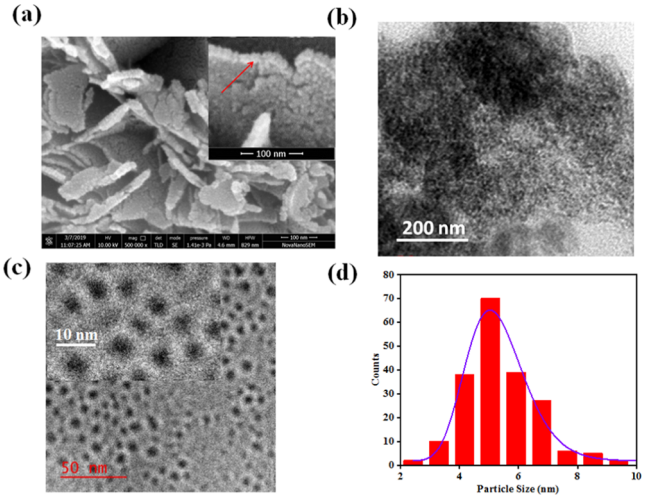

Figure 2. (a) SEM images of as-grown $CuFeS_2$ powder. The inset shows the magnified image that indicates the formation of flakes with two layers of nanocrystals. (b) TEM image of as-grown $CuFeS_2$. (c) TEM image of a dispersed colloidal $CuFeS_2$ nanocrystal. The inset shows the higher magnification image. (d) Particle size distribution as obtained from the TEM study of a dispersed colloidal $CuFeS_2$ nanocrystal.

sample for this SEM study has been prepared by spin-casting nanocrystals on a heavily doped Si substrate (p^+-Si). This SEM image indicates that the microwave-assisted $CuFeS_2$ nanostructures form flakes with a thickness of ~10−12 nm due to the formation of two layers of $CuFeS_2$ nanocrystals (inset, Figure 2a). In addition to this, transmission electron microscopy (TEM) study has been performed using an "as-grown" sample of $CuFeS_2$ that is shown in Figure 2b, which shows a micron-sized cluster that is formed by agglomerated $CuFeS_2$ nanocrystals. For this TEM study, a small amount of a powder sample of as-grown $CuFeS_2$ was dispersed in DMF and stirred for 10 min. A drop of a diluted solution of this sample was taken on a TEM grid. The rest of this solution was sonicated in an ultrasonic bath for 15 min. A drop of this sonicated $CuFeS_2$ sample was used for another set of TEM studies, which is shown in Figure 2c. Our TEM study of this sonicated sample indicates that the individual $CuFeS_2$ nanocrystals have an average size of ~5 nm (Figure 2d). This result also implies that the sonication method separates individual $CuFeS_2$ flakes and then they are disintegrated into individual nanoparticles.

2.4. Reaction Phenomena of a $CuFeS_2$ Nanocrystal. Based on our electron microscopy studies, we propose a three-step growth process of a $CuFeS_2$ nanoparticle. As mentioned earlier, at the beginning of the irradiation of microwaves, the color of the mixed precursor solution changes from bright yellow to orange. Irradiation for a longer time in the second step turns the color of the solution from orange to greenish-black. Our SEM and XRD studies have confirmed the

https://dx.doi.org/10.1021/acsomega.0c03336
ACS Omega 2020, 5, 25947−25953

formation of $CuFeS_2$ flakes that are composed of $CuFeS_2$ nanoparticles. In the third step, $CuFeS_2$ flakes disintegrate into individual $CuFeS_2$ nanoparticles under the sonication process. As a result, the nanoparticles remain in a colloidal form in the solvent. At the beginning of microwave irradiation, the temperature increases rapidly with time as the electric vector of the microwave of frequency 2.45 GHz starts interacting with the dipoles of an ethylene glycol solvent. Within thirty seconds of irradiation, the temperature of the mixture solution reaches 70 °C, whereas this temperature reaches ∼100 °C after around 80 s. When the temperature increases from 70 to 100 °C, the color of the solution changes from bright yellow to orange. It is observed that this orange color becomes more intense up to 110 s of irradiation. When the microwave irradiation is stopped at this stage, the temperature of this solution reaches close to room temperature within a couple of minutes and the color of the solution reverts to bright yellow. This observation indicates that the first step of this synthesis is a reversible process. However, the continuation of this microwave reaction shows another color change after 140 s of irradiation. This time, the deep orange color of the solution changes to greenish-black. At this stage, the temperature of the solution reaches 165 °C. After this, the solid product was separated from the solution by centrifugation at 10 000 rpm for 30 min. Then, it was dried in vacuum for 24 h at room temperature. The morphology of these powder nanoparticles observed by a high-resolution SEM (HRSEM) study shows a nanoplate structure, but after dispersion in DMF and sonication, the HRTEM image shows spherical nanoparticles with an average size of 5 nm. From these sequential observations, a growth process is proposed that is based on the "orientated attachment" model.[39,40] As soon as $CuFeS_2$ nanocrystals are formed at temperature ∼160 °C, the capping-free nanocrystals aggregate to form nanoplates spontaneously under the high-temperature condition. In this aggregated state, the nanoparticles come together and form a weak bridge that allows the solid−solid diffusion that leads to the formation of the nanoplate structure. The solution-phase ultrasonication process provides enough energy to break these nanoplates into individual nanoparticles. After sonication, the surface anion (S^{2-}) of colloidal $CuFeS_2$ nanocrystals may behave like a capping ligand around it, which restricts further agglomeration. Since the TEM samples are prepared from a sonicated solution of the nanocrystal, there is no possibility of agglomeration of nanoparticles and they are identified in TEM images.

2.5. *I*−*V* Characterization. The device performance was examined by studying the current vs voltage (I−V) characterization in the presence of white light and under dark conditions at room temperature for bilayer heterojunction and single-layer devices as shown in Figure 3a,b, respectively. Figure 3c,d show the corresponding device structure. A xenon lamp was used as a white-light source that illuminated the top side of the devices with an intensity of 100 mW/m^2. Figure 3a shows the I−V characteristics of heterojunction photoconductors. This data demonstrates that the difference of photo-to-dark current is more or less similar under different external biases with a value of ∼64, which implies excellent photosensitivity of the device. In this photodetector, ZnO and a $CuFeS_2$ nanocrystal were used as the electron-transport layer and photoactive layer, respectively. Coating of ZnO significantly improves the current from 27 to 753 μA under light, keeping the dark current approximately the same as in the $CuFeS_2$-only photodetector. The typical band alignments and

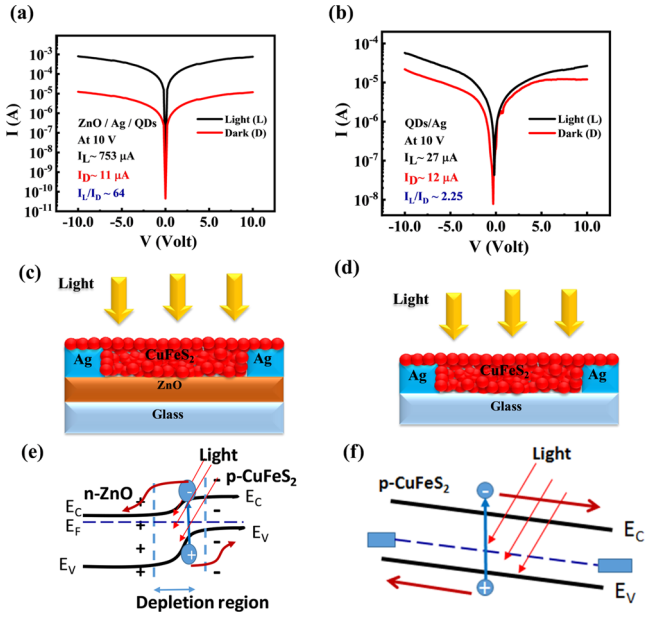

Figure 3. (a, b) Current vs voltage characteristics of the bilayer heterojunction photodetector (glass/ZnO/Ag/$CuFeS_2$) and the single-layer photodetector (glass/$CuFeS_2$/Ag). Schematic device structure of (c) the bilayer heterojunction and (d) the single-layer photodetector. Band diagram and charge transport of (e) the bilayer heterojunction device and (f) the single-layer device.

charge transport of bilayer and single-layer devices are schematically presented in Figure 3e,f, respectively. From the XRD data, it can be seen that the impurity phases of CuS and FeS having band gaps of 2.2 and 1.0 eV, respectively, coexist with pure $CuFeS_2$. However, these two impurity phases do not interfere much in the device performance for two reasons. First, both these materials are considered as semiconducting materials with reasonably good photosensitivity in the visible region of light. Besides, both these materials are p-type in nature and form a type II heterojunction with ZnO. Therefore, photogenerated electrons of the materials can easily transfer to ZnO layers like $CuFeS_2$.[41,42] Besides, due to the free "hole" carrier of CuS and FeS impurities, plasmonic absorption may arise, which is observed in the absorption spectra (Figure 1c). This plasmonic hole is metallic in nature and the plasmon oscillation frequency depends on the carrier concentration of holes according to the equation $\omega_p = \sqrt{N_h e^2/\varepsilon m_h}$ (where ω_p is the plasma frequency, N_h is the density of free holes, m_h is the effective mass of hole). Instead of exhibiting the metallic nature of this hole, the p−n heterostructure of p-CuS with an n-type semiconductor shows a superior photoresponse that has been observed earlier.[43] Similar to this, plasmonic absorption of metal nanoparticles can also generate hot electrons that can easily transfer to the neighboring metal oxide layer and enhance the photosensitivity of the device.[44]

When a photon of incident light has higher energy ($h\upsilon$) than the band gap (E_g) of the $CuFeS_2$ nanocrystal, the energy of a photon can be absorbed by the valence electrons of the nanocrystal. This absorption leads to the formation of an e^-−h^+ pair (exciton) inside the nanocrystal that experiences a force due to the existing electric field created in the depletion region formed by the heterojunction of the bilayer photodetector (Figure 3e). Due to this electric field, the electrons and holes get separated from each other, and electrons are transported through the ZnO layer, whereas holes remain in the $CuFeS_2$

https://dx.doi.org/10.1021/acsomega.0c03336
ACS Omega 2020, 5, 25947−25953

layer (Figure 3e). Because of this physical separation of charge carriers, the recombination of photogenerated carriers is considerably reduced. Moreover, the ZnO layer possesses higher carrier mobility that can transport electrons to the electrode at a much faster rate. Therefore, the bilayer heterojunction photodetector enhanced the overall conductivity of the photodetector in comparison to only $CuFeS_2$ in the photodetector. A similar phenomenon has been observed in PbS nanocrystal- and CdS nanocrystal-based photodetectors.[25,39]

2.6. Responsivity, Detectivity, and Response Time. Three important parameters of a photoconductor are responsivity (R_λ), detectivity (D^*), and external quantum efficiency (EQE) that determine the overall performance of the device in a range of electromagnetic spectra and provide the crucial information to decide on its application. The responsivity (R_λ) is the ratio of the photocurrent (I_{ph}) produced by the device to the power of the incident light (P) illuminating the effective surface area (A) of the photodetector and EQE is the number of photoelectrons generated per unit photon. On the other hand, detectivity is related to the sensitivity of the photodetector, and it is inversely proportional to the "noise equivalent power" (NEP), normalized to the per-unit detector's photosensitive area in the range of 1 Hz bandwidth. In other words, detectivity is a measure of the lowest possible value of radiant power that can generate a signal. The following mathematical relations show the interrelationship among R_λ, D^*, and EQE

$$R_\lambda = \frac{I_{ph}}{PA} \tag{1}$$

$$\mathrm{EQE} = \frac{hcR_\lambda}{e\lambda} \tag{2}$$

and

$$D^* = \frac{R_\lambda}{\sqrt{2eJ_d}} \tag{3}$$

where I_{ph} is the photocurrent at a particular applied voltage, P is the intensity of the incident light per unit area, h is Planck's constant, c is the speed of light,[39] e is the electronic charge, J_d is the dark current per unit effective area of the photodetector, and λ is the wavelength of light. In the expression of detectivity (eq 3), we have considered that the noise current is dominated by dark current only, which is a good approximation for low-intensity photodetection. Figure 4a–c show the graph of R_λ, EQE, and D^* respectively at different biasing values. Figure 4a has demonstrated its excellent photosensitivity in the range of 350–800 nm. This data also indicates that the responsivity increases with wavelength, which is a very similar trend to the absorption of the device. Moreover, this R_λ increases with external biasing, which is due to an increase in the gain of the photocurrent. The maximum value of the responsivity of this device is 43 A/W at 800 nm with the biasing of 10 V, which is a reasonably high value with respect to nanocrystal-based photodetectors.

The measured EQE values for the devices at different external biases show a very high multispectral photoresponse in the visible–NIR range as shown in Figure 4b. The EQE follows a pattern similar to that shown by the responsivity of the device. Similar to responsivity data, the EQE value is also enhanced with external bias due to the enhancement of

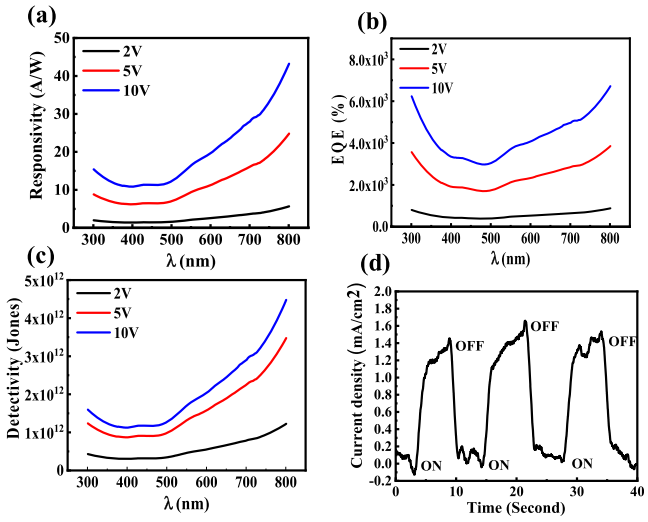

Figure 4. (a) Responsivity, (b) EQE, and (c) detectivity of a bilayer heterojunction photodetector at different biases in the spectral range of 300–800 nm. (d) Transient photoresponse of the photodetector under 5 V external bias and one sun white pulse light illumination with a repetition of 7 s.

photocurrent. This data indicates that the highest value of EQE for this photodetector is ~6717% at 800 nm under 10 V external bias. Figure 4c shows the detectivity of the device under different external biases. The highest D^* value exhibited by the device is ~4.48×10^{12} Jones at 800 nm for 10 V bias, which is reasonably high for a nanocrystal-based photodetector. These device parameters have been compared with some earlier reports that are presented in Table 1. This comparison indicates that the device performance of this photodetector is superior to those of a number of earlier studies. Therefore, this effort will be a strong addition to heavy-metal-free photodetector research.

The response time is another important characteristic of a photodetector and to characterize the speed of our device. For this study, the photodetector has been illuminated with a pulsed white-light source of one sun with a repetition interval of 7 s under 5 V external bias. The resulting transient photoresponse of the photoconductor is displayed in Figure 4d, which shows a rising and decay time of this device of 1.4 and 1.0 s, respectively. This data indicates that as a photoconductor device it has an excellent recovery time (Table 2).

3. CONCLUSIONS

In summary, we have successfully synthesized a heavy-metal-free $CuFeS_2$ nanocrystal in a short period of time via the microwave-assisted synthesis technique without using an organic ligand. TEM and SEM studies of individual steps in this synthesis indicate that nanocrystals are attached to each other during this microwave synthesis, forming nanoflakes, which is attributed to the growth of nanocrystals at high temperatures (~150 °C) and the absence of an organic ligand. However, the TEM study of this nanocrystal indicates that the ultrasonication process can successfully separate them to form a stable solution of colloidal $CuFeS_2$ nanocrystals. This data also indicates that the nanocrystals are quite uniform in size, with an average particle size of ~5 nm. Using these nanocrystals, we have successfully fabricated a bilayer p–n heterojunction photodetector with ZnO as an electron-

https://dx.doi.org/10.1021/acsomega.0c03336
ACS Omega 2020, 5, 25947–25953

Table 1. Comparison of Various Device Structures of Nanocrystal-Based Photodetectors

device	responsivity [A W^{-1}]	EQE [%]	detectivity [cm $Hz^{1/2}$ W^{-1}]	wavelength [nm]	ref
$ZnO/CuFeS_2$	43 A/W	6717	4.48×10^{12}	300−800	this work
ZnO/PbS	4.19	742	1.07×10^{11}	350−900	ACS Appl. Nano Mater 1, 6063−6072 (2018)[39]
$Bi_2Te_3-SnSe-Bi_2Te_3$	5.5	1833	6×10^{10}	370−808	Adv. Funct. Mater. 27, 1701823 (2017)[45]
$Gr-WS_2-Gr$	3.5	933	1.6×10^{10}	532	ACS Appl. Mater. Interfaces 9, 5392−5398 (2017)[46]
$Gr-WS_2-Gr$	0.1	30	NA	488−633	Science (80). 275, 1102−1106 (1997)[47]
$Gr-MoTe_2-Gr$	0.205	53.8	NA	473−1064	Nat. Nanotechnol. 6, 45−50 (2011)[48]
Ag−SnSe−Ag	8.8×10^{-8}	2.3×10^{-7}	8.7×10^{5}	473	Nanotechnology 25, 105705 (2014)[49]
ITO−SnSe−ITO	6×10^{-6}	NA	1.8×10^{7}	white light	Mater. Res. Express 3, 105038 (2016)[50]
$Ti-SnSe/WS_2-Ti$	0.099	26	1.2×10^{8}	473−1064	ACS Appl. Mater. Interfaces 8, 4781−4788 (2016)[51]

Table 2. Comparison of Device Response Time with Reported $CuFeS_2$ Nanocrystal-Based Photodetectors

type of $CuFeS_2$ nanocrystal photodetector	rise time	decay time	references
$Si/CuFeS_2$ photodiode	18 s	20 s	ACS Appl. Mater. Interfaces 2015, 7, 2235−2241[52]
$CuFeS_2$ photoconductor	5 min	3 min	J. Phys. Chem. Lett. 2018, 9, 696−701[18]
$CuFeS_2$ photoconductor	30 s	30 s	Adv. Mater. Interfaces 2020, 7, 2000056[34]
CuFeS2/ZnO photoconductor	1.4 s	1.6 s	this work

transport layer showing excellent photosensitivity in the visible and near-infrared regions. The detectivity of this photodetector reaches above 10^{12} Jones in the visible−NIR region under 10 V external bias, which is significantly high for a nontoxic nanocrystal-based photodetector.

4. EXPERIMENTAL SECTION

4.1. Synthesis of a $CuFeS_2$ Nanocrystal and a ZnO Thin Film. To synthesize a $CuFeS_2$ nanocrystal by the microwave-assisted technique, cupric acetate monohydrate (98%) and anhydrous ferric chloride were used as precursor materials. In the beginning, 50 mM copper acetate monohydrate [Cu $(CH_3COO)_2 \cdot H_2O$], 150 mM ferric chloride [$FeCl_3$], and 100 mM thiourea [CH_4N_2S] were simultaneously dissolved in 20 mL of ethylene glycol (EG). The mixture was stirred using a magnetic stirrer (1000 rpm) until all of the precursors dissolved, resulting in a dark yellow solution. The homogeneous precursor solution was subjected to 400 W microwave radiation for 5 min until the color of the solution changed from bright yellow to greenish-black. The initial color change in this synthesis process is observed to be reversible. After microwave irradiation, the precipitate was separated by centrifugation (10 000 rpm for 30 min) three times to remove larger particles and the unreacted precursors. In the first cycle, the entire product was centrifuged, which mostly removed the ethylene glycol solvent and unreacted materials. After collecting the solid product, the sample was dried and redispersed in a mixture of ethanol and acetone (1:1) and was centrifuged under the same conditions, which was repeated one more time. After this, purified $CuFeS_2$ nanocrystals were kept for 24 h for drying at room temperature in vacuum and then dissolved in dimethylformamide (DMF) at a concentration of 8 mg/mL, as it is observed that $CuFeS_2$ nanocrystals have better solubility in DMF compared to EG. Before thin-film deposition by spin-coating, the solution was agitated via a sonication process for 15 min.

To deposit a ZnO thin film, a precursor solution of zinc acetate (dihydrate) was prepared using 2-methoxyethanol as a solvent. The solution was stirred for 1 h using a magnetic stirrer to obtain a clear transparent solution of zinc acetate. After that, monoethanolamine (MEA) was added to the zinc acetate solution with a volume ratio of 1:15 to obtain the final solution with a concentration of 300 mM. The solution was kept under stirring for 6 more hours. Finally, the resultant solution was filtered with a polyvinylidene difluoride syringe filter with 0.22 μm pore size to remove bigger particles. The filtered solution was coated on a cleaned glass substrate using a spin coater, followed by an annealing process at 500° C to form a uniform thin film of ZnO.

4.2. Material Characterization. The crystal structure and phase identification of the samples were analyzed using a Rigaku X-ray diffractometer (Rigaku SmartLab 9 kW Powder type) with Cu Kα radiation (λ = 1.54 Å) in the 2θ range of 10−90° with a scan rate of 2°/min. The characterization of the microstructure of these samples was carried out by high-resolution scanning electron microscopy (HR-SEM, Nova Nano SEM 450, 30 kV) and transmission electron microscopy (TEM, Tecnai G2 20 TWIN, 200 kV). The UV−visible spectra (DRS) of different samples were recorded by a UV−visible spectrophotometer (Shimadzu UV-3600).

4.3. Device Fabrication. All photodetector devices have been fabricated on glass substrates of size 15 × 15 mm. In the beginning, all substrates were cleaned with a piranha solution that removes the organic impurity from the surface of substrates and makes them hydrophilic. After that, these substrates were cleaned by distilled water, followed by isopropyl alcohol by keeping them in an ultrasonic bath for 10 min each. Finally, the substrates were dried by blowing dry air. To deposit ZnO thin films, a precursor solution of 300 mM concentration was spin-coated at a speed of 2500 rpm for 60 s. The coated glass slides were annealed at a temperature of 350 °C for 10 min. This process was repeated two more times to obtain the desired thickness of ZnO. Finally, this ZnO thin film was kept at 500 °C for 30 min to obtain a crystalline thin film of ZnO. After ZnO deposition, parallel silver (Ag) electrodes (separation 0.45 mm and length 9 mm) of thickness 60 nm were deposited by a thermal evaporator. After the electrode deposition, a colloidal solution of a $CuFeS_2$ nanocrystal was spin-coated over the ZnO-coated substrate at a speed of 2000 rpm for 300 s. For better stacking of nanocrystal layers, ethylene-dithiol (EDT) was spin-coated over them, which also reduces the number of electron trap states of the nanocrystals. This process was repeated two times to achieve the desired thickness of nanocrystals. The schematic of the final device structure bilayer heterojunction is shown in Figure 3c. A

https://dx.doi.org/10.1021/acsomega.0c03336
ACS Omega 2020, 5, 25947−25953

reference photodetector has been fabricated without using a ZnO layer, which is shown in Figure 3d.

4.4. Electrical Characterizations and External Quantum Efficiency (EQE) Measurement. All electrical characterizations have been performed under open atmospheric conditions. During the measurements, all electrical contacts were made by a manual probe station. Electrical data was obtained by a dual-source meter (Keysight B2902A). White light was illuminated from a xenon light source. The intensity of white light was measured by a calibrated Si photodetector (Thorlabs, Inc.). The EQE of the device under bias condition was measured by illuminating the device with different wavelengths of light from a monochromator.

AUTHOR INFORMATION

Corresponding Authors

Sajal Biring − *Organic Electronics Research Center and Department of Electronic Engineering, Ming Chi University of Technology, New Taipei City 24301, Taiwan*; Email: biring@mail.mcut.edu.tw

Bhola N. Pal − *School of Materials Science and Technology, Indian Institute of Technology (Banaras Hindu University), Varanasi 221005, India; Organic Electronics Research Center and Department of Electronic Engineering, Ming Chi University of Technology, New Taipei City 24301, Taiwan*; orcid.org/0000-0001-7512-3441; Email: bnpal.mst@iitbhu.ac.in

Authors

Brajesh Kumar − *School of Materials Science and Technology, Indian Institute of Technology (Banaras Hindu University), Varanasi 221005, India*

Satya Veer Singh − *School of Materials Science and Technology, Indian Institute of Technology (Banaras Hindu University), Varanasi 221005, India*; orcid.org/0000-0002-6032-3253

Abhimanyu Chattopadhyay − *School of Materials Science and Technology, Indian Institute of Technology (Banaras Hindu University), Varanasi 221005, India*

Complete contact information is available at: https://pubs.acs.org/10.1021/acsomega.0c03336

Author Contributions

§B.K. and S.V.S. contributed equally to this work.

Notes

The authors declare no competing financial interest.

ACKNOWLEDGMENTS

This work was supported by the "Science and Engineering Research Board", India (EMR/2015/000689). The authors are grateful to the Central Instrument Facility Centre, IIT(BHU), for providing the SEM and AFM measurement facility. S.V.S. and B.K. thank IIT(BHU) for providing a Ph.D. fellowship. S.B. acknowledges the financial support from the Ministry of Science and Technology, Taiwan (MOST 109-2221-E-131-002 and 107-2221-E-131-029-MY2).

REFERENCES

(1) Litvin, A. P.; Martynenko, I. V.; Purcell-Milton, F.; Baranov, A. V.; Fedorov, A. V.; Gun'ko, Y. K. Colloidal quantum dots for optoelectronics. *J. Mater. Chem. A* **2017**, *5*, 13252−13275.

(2) Rauch, T.; Böberl, M.; Tedde, S. F.; Fürst, J.; Kovalenko, M. V.; Hesser, G.; Lemmer, U.; Heiss, W.; Hayden, O. Near-infrared imaging with quantum-dot-sensitized organic photodiodes. *Nat. Photonics* **2009**, *3*, 332−336.

(3) Cho, K.-S.; Lee, E. K.; Joo, W.-J.; Jang, E.; Kim, T.-H.; Lee, S. J.; Kwon, S.-J.; Han, J. Y.; Kim, B.-K.; Choi, B. L.; Kim, J. M. High-performance crosslinked colloidal quantum-dot light-emitting diodes. *Nat. Photonics* **2009**, *3*, 341−345.

(4) Sargent, E. H. Colloidal quantum dot solar cells. *Nat. Photonics* **2012**, *6*, 133−135.

(5) Kovalenko, M. V. Opportunities and challenges for quantum dot photovoltaics. *Nat. Nanotechnol.* **2015**, *10*, 994−997.

(6) Zhang, Q.; Yin, Y. All-Inorganic Metal Halide Perovskite Nanocrystals: Opportunities and Challenges. *ACS Cent. Sci.* **2018**, *4*, 668−679.

(7) Howes, P. D.; Chandrawati, R.; Stevens, M. M. Colloidal nanoparticles as advanced biological sensors. *Science* **2014**, *346*, No. 1247390.

(8) Rosenthal, S. J.; Chang, J. C.; Kovtun, O.; McBride, J. R.; Tomlinson, I. D. Biocompatible Quantum Dots for Biological Applications. *Chem. Biol.* **2011**, *18*, 10−24.

(9) Medintz, I. L.; Uyeda, H. T.; Goldman, E. R.; Mattoussi, H. Quantum dot bioconjugates for imaging, labelling and sensing. *Nat. Mater.* **2005**, *4*, 435−446.

(10) Kataria, M.; Yadav, K.; Haider, G.; Liao, Y. M.; Liou, Y.-R.; Cai, S.-Y.; Lin, H.-i.; Chen, Y. H.; Paul Inbaraj, C. R.; Bera, K. P.; Lee, H. M.; Chen, Y.-T.; Wang, W.-H.; Chen, Y. F. Transparent, Wearable, Broadband, and Highly Sensitive Upconversion Nanoparticles and Graphene-Based Hybrid Photodetectors. *ACS Photonics* **2018**, *5*, 2336−2347.

(11) Reiss, P.; Carrière, M.; Lincheneau, C.; Vaure, L.; Tamang, S. Synthesis of Semiconductor Nanocrystals, Focusing on Nontoxic and Earth-Abundant Materials. *Chem. Rev.* **2016**, *116*, 10731−10819.

(12) Tang, J.; Konstantatos, G.; Hinds, S.; Myrskog, S.; Pattantyus-Abraham, A. G.; Clifford, J.; Sargent, E. H. Heavy-Metal-Free Solution-Processed Nanoparticle-Based Photodetectors: Doping of Intrinsic Vacancies Enables Engineering of Sensitivity and Speed. *ACS Nano* **2009**, *3*, 331−338.

(13) Xiang, H.; Hu, Z.; Billot, L.; Aigouy, L.; Zhang, W.; McCulloch, I.; Chen, Z. Heavy-Metal-Free Flexible Hybrid Polymer-Nanocrystal Photodetectors Sensitive to 1.5 μm Wavelength. *ACS Appl. Mater. Interfaces* **2019**, *11*, 42571−42579.

(14) Zhou, H.; Hsu, W.-C.; Duan, H.-S.; Bob, B.; Yang, W.; Song, T.-B.; Hsu, C.-J.; Yang, Y. CZTS nanocrystals: a promising approach for next generation thin film photovoltaics. *Energy Environ. Sci.* **2013**, *6*, 2822−2838.

(15) Liu, Z.; Tang, A.; Wang, M.; Yang, C.; Teng, F. Heating-up synthesis of cadimum-free and color-tunable quaternary and five-component Cu−In−Zn−S-based semiconductor nanocrystals. *J. Mater. Chem. C* **2015**, *3*, 10114−10120.

(16) Dias, S.; Kumawat, K.; Biswas, S.; Krupanidhi, S. B. Solvothermal Synthesis of Cu2SnS3 Quantum Dots and Their Application in Near-Infrared Photodetectors. *Inorg. Chem.* **2017**, *56*, 2198−2203.

(17) Bhattacharyya, B.; Pandey, A. CuFeS2 Quantum Dots and Highly Luminescent CuFeS2 Based Core/Shell Structures: Synthesis, Tunability, and Photophysics. *J. Am. Chem. Soc.* **2016**, *138*, 10207−10213.

(18) Sugathan, A.; Bhattacharyya, B.; Kishore, V. V. R.; Kumar, A.; Rajasekar, G. P.; Sarma, D. D.; Pandey, A. Why Does CuFeS2 Resemble Gold? *J. Phys. Chem. Lett.* **2018**, *9*, 696−701.

(19) Bastola, E.; Bhandari, K. P.; Subedi, I.; Podraza, N. J.; Ellingson, R. J. Structural, optical, and hole transport properties of earth-abundant chalcopyrite (CuFeS2) nanocrystals. *MRS Commun.* **2018**, *8*, 970−978.

(20) García de Arquer, F. P.; Armin, A.; Meredith, P.; Sargent, E. H. Solution-processed semiconductors for next-generation photodetectors. *Nat. Rev. Mater* **2017**, *2*, 16100.

(21) Barve, A. V.; Lee, S. J.; Noh, S. K.; Krishna, S. Review of current progress in quantum dot infrared photodetectors. *Laser Photonics Rev.* **2010**, *4*, 738−750.

(22) Konstantatos, G.; Sargent, E. H. Colloidal quantum dot photodetectors. *Infrared Phys. Techn.* **2011**, *54*, 278−282.

(23) Pal, B. N.; Robel, I.; Mohite, A.; Laocharoensuk, R.; Werder, D. J.; Klimov, V. I. High-Sensitivity p−n Junction Photodiodes Based on PbS Nanocrystal Quantum Dots. *Adv. Funct. Mater.* **2012**, *22*, 1741−1748.
(24) Deng, K.; Li, L. CdS Nanoscale Photodetectors. *Adv. Mater.* **2014**, *26*, 2619−2635.
(25) Maity, P.; Singh, S. V.; Biring, S.; Pal, B. N.; Ghosh, A. K. Selective near-infrared (NIR) photodetectors fabricated with colloidal CdS:Co quantum dots. *J. Mater. Chem. C* **2019**, *7*, 7725−7733.
(26) Deng, Z.; Jeong, K. S.; Guyot-Sionnest, P. Colloidal Quantum Dots Intraband Photodetectors. *ACS Nano* **2014**, *8*, 11707−11714.
(27) Lim, H.; Tsao, S.; Zhang, W.; Razeghi, M. High-performance InAs quantum-dot infrared photodetectors grown on InP substrate operating at room temperature. *Appl. Phys. Lett.* **2007**, *90*, No. 131112.
(28) Gunapala, S. D.; Levine, B. F.; Ritter, D.; Hamm, R. A.; Panish, M. B. Lattice-matched InGaAsP/InP long-wavelength quantum well infrared photodetectors. *Appl. Phys. Lett.* **1992**, *60*, 636−638.
(29) Conejeros, S.; Alemany, P.; Llunell, M.; Moreira, I. dP. R.; Sánchez, V.; Llanos, J. Electronic Structure and Magnetic Properties of CuFeS2. *Inorg. Chem.* **2015**, *54*, 4840−4849.
(30) Zhang, Z.; Xu, B.; Zhang, L.; Ren, S. Hybrid Chalcopyrite−Polymer Magnetoconducting Materials. *ACS Appl. Mater. Interfaces* **2016**, *8*, 11215−11220.
(31) Wu, Y.; Zhou, B.; Yang, C.; Liao, S.; Zhang, W.-H.; Li, C. CuFeS2 colloidal nanocrystals as an efficient electrocatalyst for dye sensitized solar cells. *Chem. Commun.* **2016**, *52*, 11488−11491.
(32) Gabka, G.; Zybała, R.; Bujak, P.; Ostrowski, A.; Chmielewski, M.; Lisowski, W.; Sobczak, J. W.; Pron, A. Facile Gram-Scale Synthesis of the First n-Type CuFeS2 Nanocrystals for Thermoelectric Applications. *Eur. J. Inorg. Chem.* **2017**, *2017*, 3150−3153.
(33) Ghosh, S.; Avellini, T.; Petrelli, A.; Kriegel, I.; Gaspari, R.; Almeida, G.; Bertoni, G.; Cavalli, A.; Scotognella, F.; Pellegrino, T.; Manna, L. Colloidal CuFeS2 Nanocrystals: Intermediate Fe d-Band Leads to High Photothermal Conversion Efficiency. *Chem. Mater.* **2016**, *28*, 4848−4858.
(34) Sugathan, A.; Saigal, N.; Rajasekar, G. P.; Pandey, A. Copper Iron Sulfide Nanocrystal-Bulk Silicon Heterojunctions for Broadband Photodetection. *Adv. Mater. Interfaces* **2020**, *7*, No. 2000056.
(35) Layek, A.; Middya, S.; Dey, A.; Das, M.; Datta, J.; Banerjee, C.; Ray, P. P. Study of resonance energy transfer between MEH-PPV and CuFeS2 nanoparticle and their application in energy harvesting device. *J. Alloys Compd.* **2014**, *613*, 364−369.
(36) Xie, Y.; Riedinger, A.; Prato, M.; Casu, A.; Genovese, A.; Guardia, P.; Sottini, S.; Sangregorio, C.; Miszta, K.; Ghosh, S.; Pellegrino, T.; Manna, L. Copper Sulfide Nanocrystals with Tunable Composition by Reduction of Covellite Nanocrystals with Cu+ Ions. *J. Am. Chem. Soc.* **2013**, *135*, 17630−17637.
(37) Luther, J. M.; Jain, P. K.; Ewers, T.; Alivisatos, A. P. Localized surface plasmon resonances arising from free carriers in doped quantum dots. *Nat. Mater.* **2011**, *10*, 361−366.
(38) Liu, X.; Wang, X.; Zhou, B.; Law, W.-C.; Cartwright, A. N.; Swihart, M. T. Size-Controlled Synthesis of Cu2-xE (E = S, Se) Nanocrystals with Strong Tunable Near-Infrared Localized Surface Plasmon Resonance and High Conductivity in Thin Films. *Adv. Funct. Mater.* **2013**, *23*, 1256−1264.
(39) Paliwal, A.; Singh, S. V.; Sharma, A.; Sugathan, A.; Liu, S.-W.; Biring, S.; Pal, B. N. Microwave-Polyol Synthesis of Sub-10-nm PbS Nanocrystals for Metal Oxide/Nanocrystal Heterojunction Photodetectors. *ACS Appl. Nano Mater.* **2018**, *1*, 6063−6072.
(40) Thanh, N. T. K.; Maclean, N.; Mahiddine, S. Mechanisms of Nucleation and Growth of Nanoparticles in Solution. *Chem. Rev.* **2014**, *114*, 7610−7630.
(41) Basu, M.; Garg, N.; Ganguli, A. K. A type-II semiconductor (ZnO/CuS heterostructure) for visible light photocatalysis. *J. Mater. Chem. A* **2014**, *2*, 7517−7525.
(42) Wang, D.-Y.; Jiang, Y.-T.; Lin, C.-C.; Li, S.-S.; Wang, Y.-T.; Chen, C.-C.; Chen, C.-W. Solution-Processable Pyrite FeS2 Nanocrystals for the Fabrication of Heterojunction Photodiodes with Visible to NIR Photodetection. *Adv. Mater.* **2012**, *24*, 3415−3420.
(43) Hassan, M. S.; Bera, S.; Gupta, D.; Ray, S. K.; Sapra, S. MoSe2−Cu2S Vertical p−n Nanoheterostructures for High-Performance Photodetectors. *ACS Appl. Mater. Interfaces* **2019**, *11*, 4074−4083.
(44) Singh, S. V.; Kumar, M. P.; Anantharaj, S.; Mukherjee, B.; Kundu, S.; Pal, B. N. Direct Evidence of an Efficient Plasmon-Induced Hot-Electron Transfer at an in Situ Grown Ag/TiO2 Interface for Highly Enhanced Solar H2 Generation. *ACS Appl. Energy Mater.* **2020**, *3*, 1821−1830.
(45) Yao, J.; Zheng, Z.; Yang, G. All-Layered 2D Optoelectronics: A High-Performance UV−vis−NIR Broadband SnSe Photodetector with Bi2Te3 Topological Insulator Electrodes. *Adv. Funct. Mater.* **2017**, *27*, No. 1701823.
(46) Zhang, K.; Fang, X.; Wang, Y.; Wan, Y.; Song, Q.; Zhai, W.; Li, Y.; Ran, G.; Ye, Y.; Dai, L. Ultrasensitive Near-Infrared Photodetectors Based on a Graphene−MoTe2−Graphene Vertical van der Waals Heterostructure. *ACS Appl. Mater. Interfaces* **2017**, *9*, 5392−5398.
(47) Nie, S.; Emory, S. R. Probing Single Molecules and Single Nanoparticles by Surface-Enhanced Raman Scattering. *Science* **1997**, *275*, 1102.
(48) Shimizu, T.; Haruyama, J.; Marcano, D. C.; Kosinkin, D. V.; Tour, J. M.; Hirose, K.; Suenaga, K. Large intrinsic energy bandgaps in annealed nanotube-derived graphene nanoribbons. *Nat. Nanotechnol.* **2011**, *6*, 45.
(49) Cao, J.; Wang, Z.; Zhan, X.; Wang, Q.; Safdar, M.; Wang, Y.; He, J. Vertical SnSe nanorod arrays: from controlled synthesis and growth mechanism to thermistor and photoresistor. *Nanotechnology* **2014**, *25*, No. 105705.
(50) Pawbake, A. S.; Jadkar, S. R.; Late, D. J. High performance humidity sensor and photodetector based on SnSe nanorods. *Mater. Res. Express* **2016**, *3*, No. 105038.
(51) Jia, Z.; Xiang, J.; Wen, F.; Yang, R.; Hao, C.; Liu, Z. Enhanced Photoresponse of SnSe-Nanocrystals-Decorated WS2 Monolayer Phototransistor. *ACS Appl. Mater. Interfaces* **2016**, *8*, 4781−4788.
(52) Wang, W.; Jiang, J.; Ding, T.; Wang, C.; Zuo, J.; Yang, Q. Alternative Synthesis of CuFeSe2 Nanocrystals with Magnetic and Photoelectric Properties. *ACS Appl. Mater. Interfaces* **2015**, *7*, 2235−2241.

https://dx.doi.org/10.1021/acsomega.0c03336
ACS Omega 2020, 5, 25947−25953